ICHE 2014, Hamburg - Lehfeldt & Kopmann (eds) - © 2014 Bundesanstalt für Wasserbau ISBN 978-3-939230-32-8

Numerical Simulation of Turbulent Free Surface Flow Around a Circular Cylinder

J. Paik
Gangneug-Wonju National University, Gangneung, Gangwon, Korea

F.A. Bombardelli
University of California, Davis, CA, USA

N.-J. Lee
Kyungsung University, Pusan, Korea

ABSTRACT: Flow past a surface-piercing cylindrical structure exhibits a substantial amount of free-surface variation along the obstacle surface at high Froude numbers. The free-surface variations and the corresponding pressure gradient result in a remarkable downward flow with a strong velocity component in the radial direction. The interactions of turbulent vortical structures with the free-surface as well as the cylinder and bottom wall are numerical investigated for a turbulent flow past a circular cylinder in a rectangular channel. The flow was experimentally investigated by Graf and Yulistiyanto (1998) at the Reynolds number of 1.48×10^5 and at the Froude number of 0.5. The turbulent flow is modeled using the URANS approach with the standard k-ε and the k-ω shear stress transport (SST) turbulent models along with the scale-adapted simulation (SAS) approach based on the SST model. A two-phase volume of fluid technique is employed to simulate the variation of free-surface. The comparison of numerical prediction with the measurements shows that the free-surface variation around the cylinder can be reasonably captured by all numerical models. It demonstrates that the numerical prediction of the free-surface around obstacle is not sensitive to turbulence models applied in this study. Although the size of the mean horseshoe vortex at the front and the lee-wake vortex at the downstream of the obstacle are differently predicted, all numerical solutions appear to reasonably reproduce the mean flow fields including the distinct counterclockwise circulation at the downstream side of the cylinder that was observed in the experiments. The turbulent kinetic energy (TKE) distributions around the obstacle are underestimated by URANS computations with wall functions. Even though its magnitude is still underestimated, the URANS with wall-integration yields better prediction of TKE, especially in the wake region. The preliminary high resolution SAS simulation demonstrates that the scale-resolving simulation improves the numerical prediction in terms of mean flow and turbulence statistics.

Keywords: Turbulent flow, Free surface, Cylinder, Numerical simulation

1 INTRODUCTION

The flow past a wall-mounted cylindrical obstacle is dominated by the horseshoe vortex and the lee-wake vortical structure. Due to the presence of the adverse pressure gradient induced by the obstacle, the approaching turbulent boundary layer undergoes a three-dimensional separation leading to the formation of a complex horseshoe vortex system around the obstacle. The strongly turbulent horseshoe vortex system produces a high bed-shear stress underneath of the primary vortex. The turbulent horseshoe vortex typically reveals the presence of an elongated pocket of intense positive turbulence kinetic energy (TKE) production in the vicinity of the vortex system (Devenport & Simption 1990). The lee-wake vortices are caused by the rotation in the boundary layer over the cylinder surface. The shear layers emanating from the side edges of the cylinder roll up to form these vortices in the lee-wake of the obstacle (Sumer & Fredsøo 1997). Flow past the surface-piercing cylindrical structure exhibits a substantial amount of free-surface variation in the vicinity of the structure along with a run-up in the front and a depression around the side edge and at the back at high Froude number (*Fr*). When the *Fr* is large, the combination of the Reynolds stress anisotropy and the free-surface fluctuations makes a significant contribution on the flow in the vicinity of the obstacle (Graf & Yulistiyanto 1998, Rouland et al 2005).

Turbulence models most widely used in recent hydraulic engineering tools to simulate flow around bottom mounted cylindrical obstacles are unsteady Reynolds-averaged Navier-Stokes (URANS) model employing the standard $k-\varepsilon$ (Liu & Garcia 2008), a nonlinear $k-\varepsilon$ (Nagata et al. 2003), the Wilcox's k-ω (Khosronejad et al. 2012), the k-ω shear stress transport (SST) model (Rouland et al. 2005), or the Reynolds stress model (Salaheldin et al. 2004). Notwithstanding the fact that URANS computations in general fail to capture the location and the shape of the mean horseshoe vortex (Apsley & Leschziner 2001), URANS approach is considered as a practical hydraulic engineering tool due to the huge discrepancy of time-scales between the coherent structures and other flow processes, like scour. It should be noted that all aforementioned URANS computations were applied for the low *Fr* (≤ 0.2) flows. Overall mean properties of the flow around the cylinder can be captured even with the rigid-lid free-surface condition, provided that the *Fr* is small enough. For high *Fr* flow, however, the appropriate modeling of the free-surface along with employing advanced turbulence modeling technique is essential to accurately reproduce the flow around obstacle. For example, Rouland et al. (2005) demonstrated that the numerical modeling with the rigid-lid approximation of the free-surface cannot capture even mean radial velocity fields at the side and behind of the cylinder at the *Fr* of 0.5.

The large eddy simulation (LES) is the most advanced engineering technique to resolving the flow at affordable Reynolds number (Re). Recent LES of flow around a circular cylinder have focused on flows over the geometrically two-dimensional obstacle (Parnaudeau et al. 2008, Lysenko et al. 2012). LES of flows past a free-surface piercing circular cylinders were also conducted (Kawamura et al. 2002, Yu et al. 2008). However, their studies concentrated on the flow at low Reynolds numbers, where the bottom wall was treated with the slip, symmetric boundary condition. Large eddy simulation of wall bounded flows at practical Re will not be feasible within the near future. Over the last decade, hybrid RANS/LES is emerging into a useful and powerful engineering simulation tool to simulate a wide range of complex flows at high Re. Detached eddy simulation (DES) developed by Spalart et al. (1997) of turbulent flow around wall-mounted cylinders were carried out at high Re, which elucidated the distinct mechanism of horseshoe vortex induced by the three-dimensional boundary-layer separation and the strong interaction of vortical structures with the cylinder and bottom walls (Paik et al. 2007, Kirkil et al. 2009, Escauriaza and Sotiropoulos 2011). These works, however, were carried out with the flat, rigid-lid assumption of the free-surface at low *Fr*. More recently developed scale adaptive simulation (SAS) operates in the so-called scale-resolving simulation mode which automatically balances the contributions of modeled and resolved parts of the turbulent stresses (Menter & Egorov 2010). The SAS model changes smoothly from a LES mode to a RANS mode through various stages of eddy resolution. The SAS behaves in many situations similar to the DES, but has no an explicit influence of the grid spacing on the RANS mode which allows for a safer passage from RANS to SRS, especially for complex applications where high quality LES meshes can't easily be generated for the detached flow regions (Egorov et al. 2010).

The objective of the present work is twofold. The first is to investigate the performance of the URANS computations employing widely used two-equation turbulence models, such as the standard *k-ε* and the *k-ω* SST models to reproduce free-surface variation and flow behavior around a free-surface-piercing cylinder at the *Fr* of 0.5. The second is to test the performance of the SAS approach to the same flow and to study the effect of the scale-resolving turbulence modeling on the flow in the vicinity of the cylinder. We further study the sensitivity of numerical solutions to the wall boundary conditions by employing two different computational meshes for wall-function and wall-integration calculations.

2 NUMERICAL METHODS

2.1 *Governing Equations*

The governing equations for the mean flow are the unsteady, incompressible Reynolds-averaged Navier-Stokes (RANS) equations.:

$$\nabla \cdot (\mathbf{u_f}) = 0 \tag{1}$$

$$\frac{\partial \rho_f \mathbf{u_f}}{\partial t} + \nabla \cdot (\rho_f \mathbf{u_f} \mathbf{u_f}) = -\nabla p_{rgh} + (\mathbf{g} \cdot \mathbf{x}) \nabla \rho_f + \nabla \cdot (\boldsymbol{\tau}) + \mathbf{F_b} \tag{2}$$

where the tensor product $\mathbf{u_f u_f} = u_i u_j \mathbf{e_i e_j}$, and $\mathbf{F_b}$ is the external force term. The only difference from the original RANS equations is that the piezometric pressure $p_{rhg} = p - \rho_f \mathbf{g} \cdot \mathbf{x}$ where $\mathbf{x}$ is the coordinate vector and ρ_f is the density of fluid is solved instead of the pressure p. Hence the term $-\nabla p + \rho_f \mathbf{g}$ in the momentum equation of the vector form of RANS equations is re-written as $-\nabla p_{rhg} - (\mathbf{g} \cdot \mathbf{x}) \nabla \rho_f$.

The free-surface variation is significant at the present high Fr. The interface of water-air fluids is captured by means of the two-phase volume of fluid (VOF) method. The location of the free-surface is obtained by the volume of faction α_1, calculated by solving its transport equation with an artificial surface compression term (Weller 2008).

$$\frac{\partial \alpha_1}{\partial t} + \nabla \cdot (\alpha_1 \mathbf{u_f}) - \nabla \cdot (\alpha_1 (1 - \alpha_1) \mathbf{u_{r\alpha}}) = 0 \tag{3}$$

where $\mathbf{u_{r\alpha}}$ is the compression velocity accounting for the global maximum value of the velocity field. This additional convective term in the phase fraction equations is introduced to suppress the smearing of steep gradients induced by the numerical diffusion. In this study, the compression coefficient controlling the intensity of the free-surface compression is set to 1.0 which corresponding to the conservative compression.

Two turbulence modeling approaches are taken into account in this study: the URANS computations with the $k-\omega$ shear stress transport (SST) model and the scale-adaptive simulation (SAS) based on the $k-\omega$ SST model. The standard $k-\varepsilon$ model is also considered in the URANS modeling for the comparison. Due to the space limitation, the model equations are not included and a brief summary of modeling concept is introduced in this section. The $k-\omega$ SST model was developed by Menter (1994) to improve Wilcox's original model so that an even higher sensitivity could be obtained for flows encountering the adverse pressure gradient. The SST model is a blend of a $k-\omega$ model used for flow near walls, and a $k-\varepsilon$ model for flow in region far from walls. This model is fairly robust and generally yields a good solution near solid boundaries. It is also often found to do a better job at capturing recirculation regions than other models (Menter 1994). For this reason, the $k-\omega$ SST model has been chosen for the present application in which there is a strong adverse pressure effect which is responsible for the formation of the horseshoe vortex in the vicinity of the obstacle.

The scale-adaptive simulation (SAS) concept is described in much detail in the cited reference Menter & Egorov (2010). The difference between the standard RANS and SAS models lies in the treatment of the scale-defining equation. In traditional RANS models, the scale equation is modeled based on an analogy with the k-equation using simple dimensional arguments. The scale equation of the SAS model is based on an exact transport equation for the turbulence length scale. The introduction of the von Karman length scale into the system of equations allows the model to adjust its behavior to resolved scales. This method was re-visited by Menter & Egorov (2010) and avoids some limitations of the original Rotta's model. As the flow exhibits sufficient inherent instabilities and the computational mesh is sufficiently refined, the source term including the von Karman length scale is activated and dominates the other terms, yielding the full activation of the SAS functionality. The resulting SAS model behaves in many flows similarly to DES, but with less explicit impact of the grid spacing on the model formulation (Egorov et al. 2010).

2.2 *Numerical Approaches*

The governing equations are solved numerically by means of the finite volume method implemented in the open source CFD toolkit, called OpenFOAM. Overall fully second-order-accurate setup both in time and in space is used for the simulations. PIMPLE pressure-velocity coupling algorithm is used. The generalized second-order-accurate backward, implicit, differencing scheme is used to evaluate the time derivatives. Spatial discretization for the convective term is achieved using a high- resolution (bounded central) difference scheme based on normalized variable diagram (NVD), called by Gamma scheme. This scheme is bounded by blending the second-order central difference and the first-order upwind schemes. The smooth transition between two schemes is controlled by the blending coefficient which has a value in the range between 0.1 and 0.5. Smaller value provides a good resolution (less diffusive) solution, while high value is more numerically stable. In this study the value of the blend coefficient is set to 0.1.

One of the major difficulties in the VOF method is ensuring the transport of sharp interfaces without artificial numerical diffusion or dispersion. In the VOF model, the boundedness of volume faction is maintained by utilizing a bounded central differencing (Limited Linear) scheme combined with a solution procedure referred to as multi-dimensional universal limiter for explicit solution (MULES).The number of sub-cycles for the volume fraction for each physical time-step is set to 4 and the number of correction loops over the volume fraction is set to 2.

3 COMPUTATIONAL DETAILS

The flow field around a bottom-mounted, surface piercing cylinder in an open channel has been experimentally investigated by Graf & Yulistiyanto (1998) at the Froude number of 0.5 and the Reynolds number of 1.48×10^5, based on the free-stream mean velocity of U = 0.67 m/s and the cylinder diameter D = 0.22 m. In the experiment, the 0.5 m high cylinder was installed normal to the 0.185 m deep flow at the symmetric plane at x = 16 m downstream of the flume entrance. The experiment flume is 2m wide and has with a constant slope of 6.25×10^{-4}. The flow approaching the cylinder experiences a three-dimensional boundary layer separation. Graf & Yulistiyanto (1998) observed that the resulting flow at the upstream of the cylinder is characterized by the horseshoe vortex system and is reasonably organized while the lee-wake vortex flow mush less organized at the downstream of the pier. They observed the largest values of the bed shear stress at the 45° plane. The difference between the surface elevation in front and at the side edge of the pier is approximately Δh = 5.2 cm at Fr = 0.5. The depth difference and the resulting pressure gradient along the free-surface generate a remarkable down- and outward flow with strong component of flow velocity in the radial direction. The measurements also show that considerable turbulence is associated with the fluctuating components of the necklace-like horseshoe vortex at the front and side of the cylinder and lee-wake vortices behind of the obstacle. Note, however, Graf & Yulistiyanto (1998) reported that no clear conclusive trend of turbulence statistics near the bed is detectable, since all measurements near the bed are doubtful due to the limitation of the measuring technique.

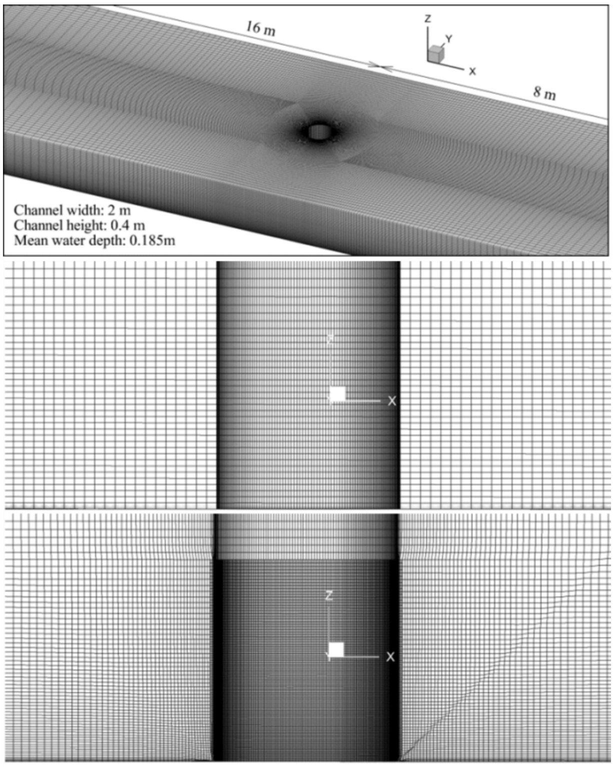

Figure 1. Computation meshes: [upper] 3D view of mesh around a cylinder, [middle] grid resolution of the WF mesh for wall function computation, [lower] grid resolution of the WI mesh for wall integration computations.

The present computational domain considers the full width (9.1D) of the experimental channel and both side walls are treated as the no-slip boundary. To eliminate the assumption of inflow conditions, the computational domain is extended 16 m upstream of the cylinder center which is same to the experimental configurations. The outlet is specified at 8 m (36.4 D) downstream of the cylinder.

Two different meshes are used to study the sensitivity of numerical model to the mesh resolution and wall boundary conditions: the coarse mesh for wall-function computation (hereafter referred to as “WF”) and the fine mesh for wall integration computation (referred to as “WI”). The body-fitted, structure grids are generated for all solid walls. The WF mesh consists of 1.22×10^6 computational cells and the first node off-the-wall is located in the logarithmic layer ($y^+ \sim 80$) for computation with wall functions. The WI mesh for the wall-integration computation is generated by stretching the mesh only near the cylinder surface and bottom wall, and adding 5 layers along these solid boundaries where y^+ value at the center of the first cell off the wall is set to 1. The total number of the fine mesh cells is 3.40×10^6. In both meshes, the side wall boundary is treated by wall functions. The physical time-marching steps are 0.006 D/U_o and 0.0015 D/U_o for the coarse and the fine mesh calculations, respectively.

The computational domain consists of four boundaries: inlet, outlet, solid wall and atmosphere. The inlet plane consists of the lower water section and the upper air section. The volume faction α_1 is set to 1 and 0 for the water flow and the air flow, respectively. The uniform mean measured velocity is applied for the water flow at the inlet for all computations, while the zero gradient boundary condition is imposed to air flow at the inlet. Inlet boundary condition on pressure is zero gradient. The turbulence quantities of k and ω at the inlet are set the values obtained by using the turbulent length scale which is set to 7% of the hydraulic diameter and the turbulent intensity of 2.5% of the mean velocity. At the outlet and top atmospheric boundaries, zero-gradient Neumann condition applied for scalar and vector quantities except pressure for the water flow. The hydrostatic pressure boundary condition is applied for the water flow at the outlet. No-slip boundary condition is applied to all wall boundaries. Turbulence quantities are defined through wall functions. The volume fraction at the wall is calculated by the zero-gradient condition.

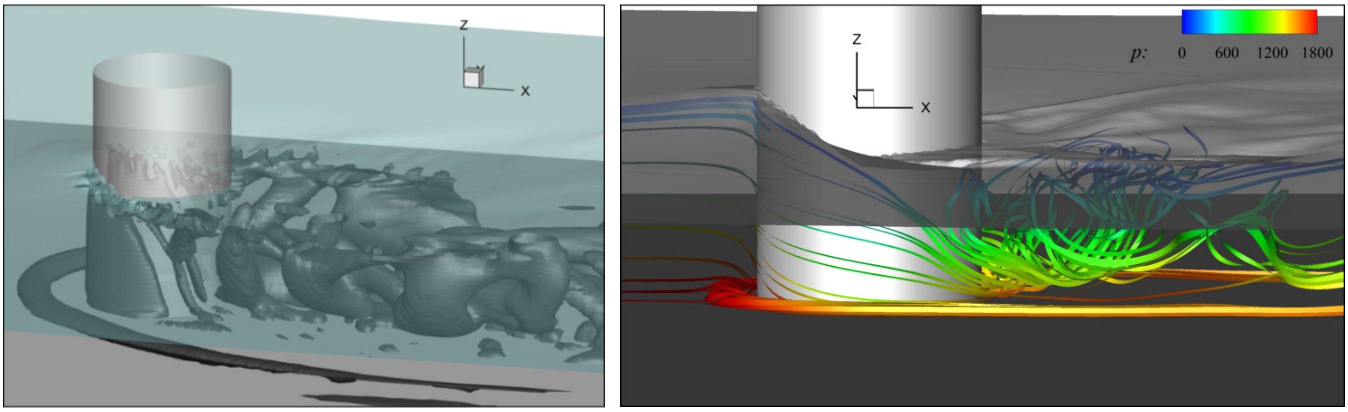

Figure 2. Snapshot of instantaneous flow field around the cylinder computed by the SAS-WI: [*left*] free-surface variation visualized by the iso-surface of the volume fraction and coherent structures identified by the iso-surface of Q criterion and [*right*] free-surface and horseshoe and lee-wake vortices identified by streamlines colored by pressure.

4 RESULTS

We first present a few instantaneous numerical results concerning the free-surface variation and the coherent structure dynamics of the horseshoe and the lee-wake vortices of the flow. It is followed by the comparison of numerical predictions of time-averaged mean velocity vectors and turbulent kinetic energy (TKE) distributions with the experimental observations of Graf & Yulistiyanto (1998) at the symmetric planes at the front and the behind of the cylinder. For convenience, each numerical solutions presented in this study is dubbed as the combined name of the turbulence mode and the computational mesh: e.g. the URANS with the SST model on the WF (coarse) mesh as SST-WF and the SAS solution obtained on the fine (WI) mesh as SAS-WI.

Figure 2 shows the free-surface variation visualized by the iso-surface of the volume fraction and the horseshoe and the lee-wake vortical structures identified by the iso-surface of Q-criterion ($Q = S^2 - \Omega^2$ where S is the strain rate and Ω is the vorticity) in the vicinity of the cylinder. The necklace-like vortical structure near the bed in the front of the cylinder is the horseshoe vortex generated by the three-dimensional separation of the approaching boundary layer induced by the present of the adverse pressure gradient. Since the mesh resolution is not sufficiently fine, the present numerical solution does not yield the distinct bi-modal mechanism of the horseshoe vortex with intense unsteadiness. The lee-wake vortices are captured in the wake which caused by the rotation in the boundary layer over the cylinder surface. The shear layers emanating from the side edges of the cylinder roll up to form these vortices in the lee wake of the obstacle (Sumer & Fredsøe 1997). The figure confirms that the present numerical simulation reasonably reproduces the lee-wake vortical structures observed in the near wake.

The streamlines launched inside the approaching boundary layer merge together and form the horseshoe vortex wrapping the cylinder, as seen in Figure 2. A significant amount of the free-surface variation along the cylinder surface is further obvious in this figure where there is a run-up at the front and a strong depression at the side and at the back of the cylinder. The streamlines clearly show that a strong down flow is occurring along the cylinder surface which is obviously due to the pressure gradient induced by the water depth difference. These streamlines display the very

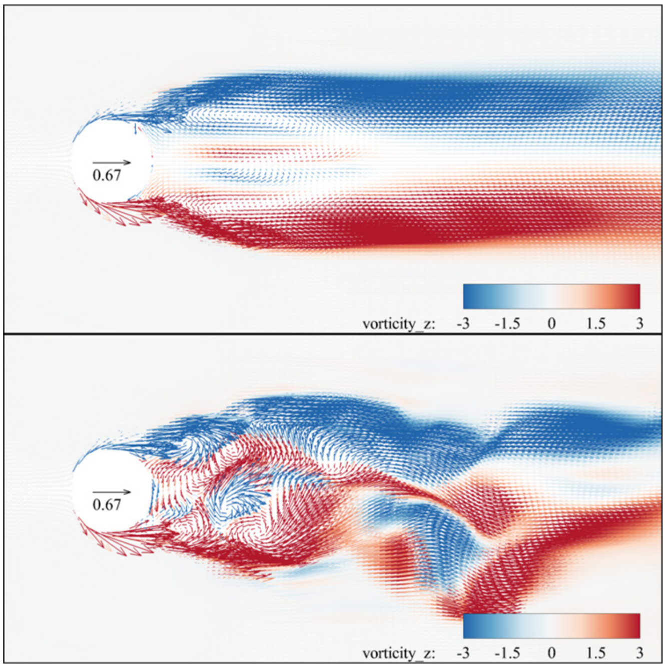

Figure 3. Snapshots of instantaneous velocity vectors colored by out-of-plane vorticity computed by [*upper*] SST-WI model and [*lower*] SAS-WI at the plane of the mid-depth ($z = 0.5H$).

complex lee-wake vortices in the wake. Interestingly, the flow field computed near the free-surface along the cylinder is not significantly sensitive to the turbulence models employed in this study. The difference between the computed water surface elevations at the front and the side of cylinder ranges from 0.047 m (SAS-WF) to 0.060 m (k-ε-WF). These numerical predictions are comparable to the measured value of 0.052 m.

Figure 3 shows instantaneous snapshots of velocity vectors at the mid-depth (z = 0.5H) horizontal plane obtained by the SST-WI and the SAS-WI computations. It is noteworthy in the figure that URANS computation (SST-WI) has failed to capture the oscillating behavior of the lee-wake vortical structures in the spanwise direction and yields a single mode, quasi-steady-state wake structure. The SAS-WI reveals that the lee-wake flow consists of multiple vortices shed from the separation point of the cylinder surface and can be characterized by a low-frequency large scale oscillation of a bunch of these vortices.

The instantaneous velocity vector and vorticity fields computed near the bed reveal the unsteady behavior of coherent vertical structures of which features are similar to those observed at the mid-depth. The URANS solution shows the footprint of a quasi-steady-state, single mode horseshoe vortex wrapping the cylinder and vertical structures with very weak unsteadiness in the wake region. The SAS allows the formation of turbulent lee-wake structures, which cannot be observed in the URANS solutions, while the trace of horseshoe vortex is rather weekly computed at the horizontal plane (z=0.03H). The results is attributable to that the tail of the necklace-like vortex keeps further away from the bed as it moves to downstream, which is presumably due to the flapping motion of the lee-wake structure in the SAS solutions.
Time-averaged velocity vectors and the total (modeled + resolved) TKE distributions computed at the

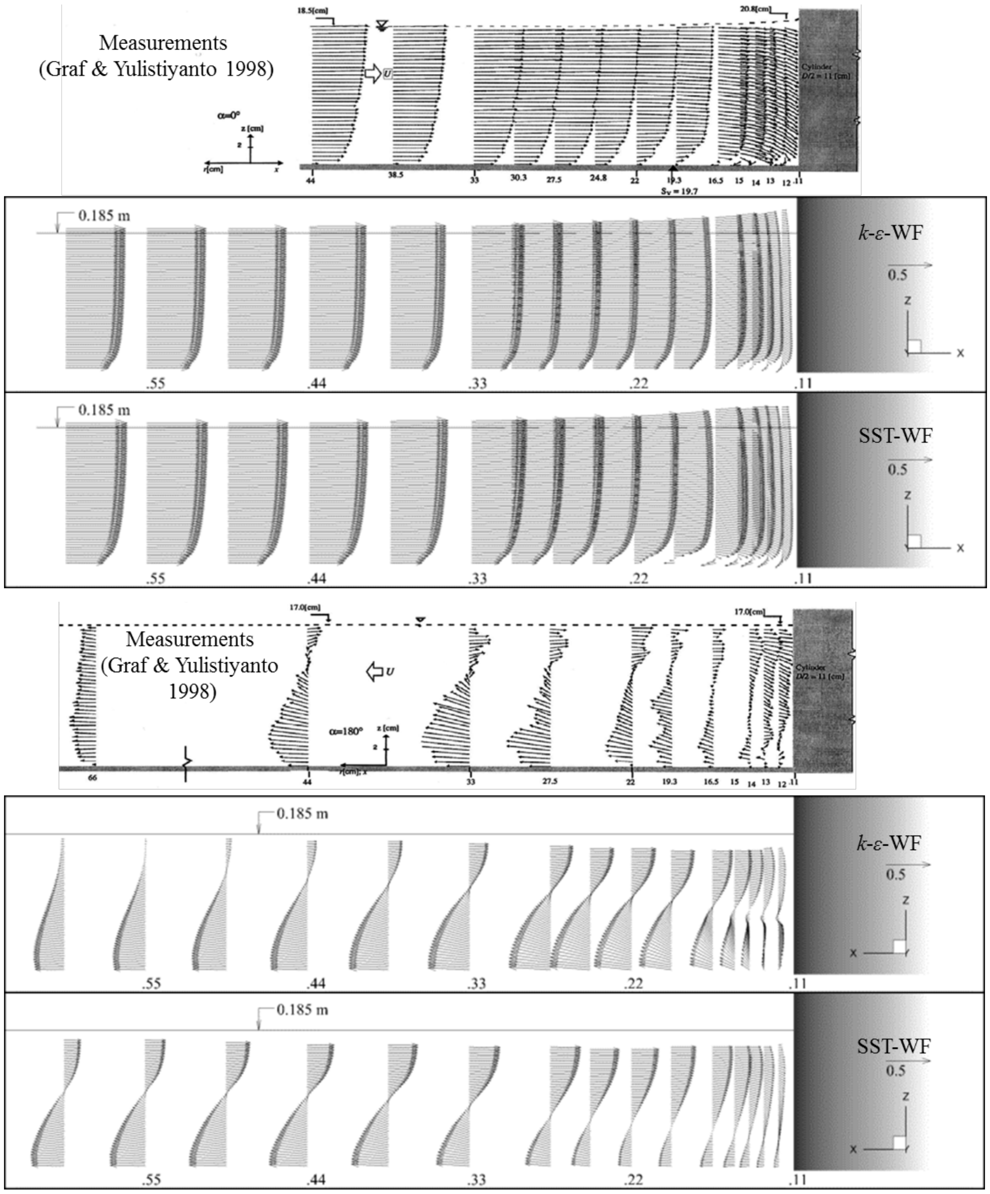

Figure 4. Comparison of measurement (Graf & Yulistiyanto 1998) and numerical prediction of time-averaged velocity vectors at the symmetric planes of [upper] upstream and [lower] downstream of the cylinder.

plane of symmetry upstream and downstream of the cylinder are compared with the experimental measurements in Figure 5. Due to the space limitation, only URANS solution employing the standard k-ε and the SST models are included in these figure. The separation point of the approaching boundary layer was observed at x = 0.197 m upstream of the cylinder in the experiments. The k-ε-WF computation underestimates the separation point approximately at x = 0.15 m while the SST-WF and SST-WI computations reasonably well predict the separation point at x = 0.21 m and 0.22 m, respectively. All numerical solutions appear to yield time-averaged velocity vector fields which are comparable to each other at the front of the cylinder. However, rather different velocity fields are computed at the symmetric plane in the wake. Interestingly, all present numerical simulations can reasonably reproduce the free-surface variation and the resulting strong radial component of the flow observed by Graf & Yulistiyanto (1998). The overall feature of the time-averaged recirculating flow in the wake region is reasonably captured by all computations. Recall that the SST-WI computation conducted by Rouland et al. (2005) with the rigid-lid assumption for the free-surface failed to capture this distinct feature of the wake flow. It confirms that the resolving of the free-surface is essential to accurately reproduce the flow in the vicinity of the cylinder at the given *Fr* of 0.5.

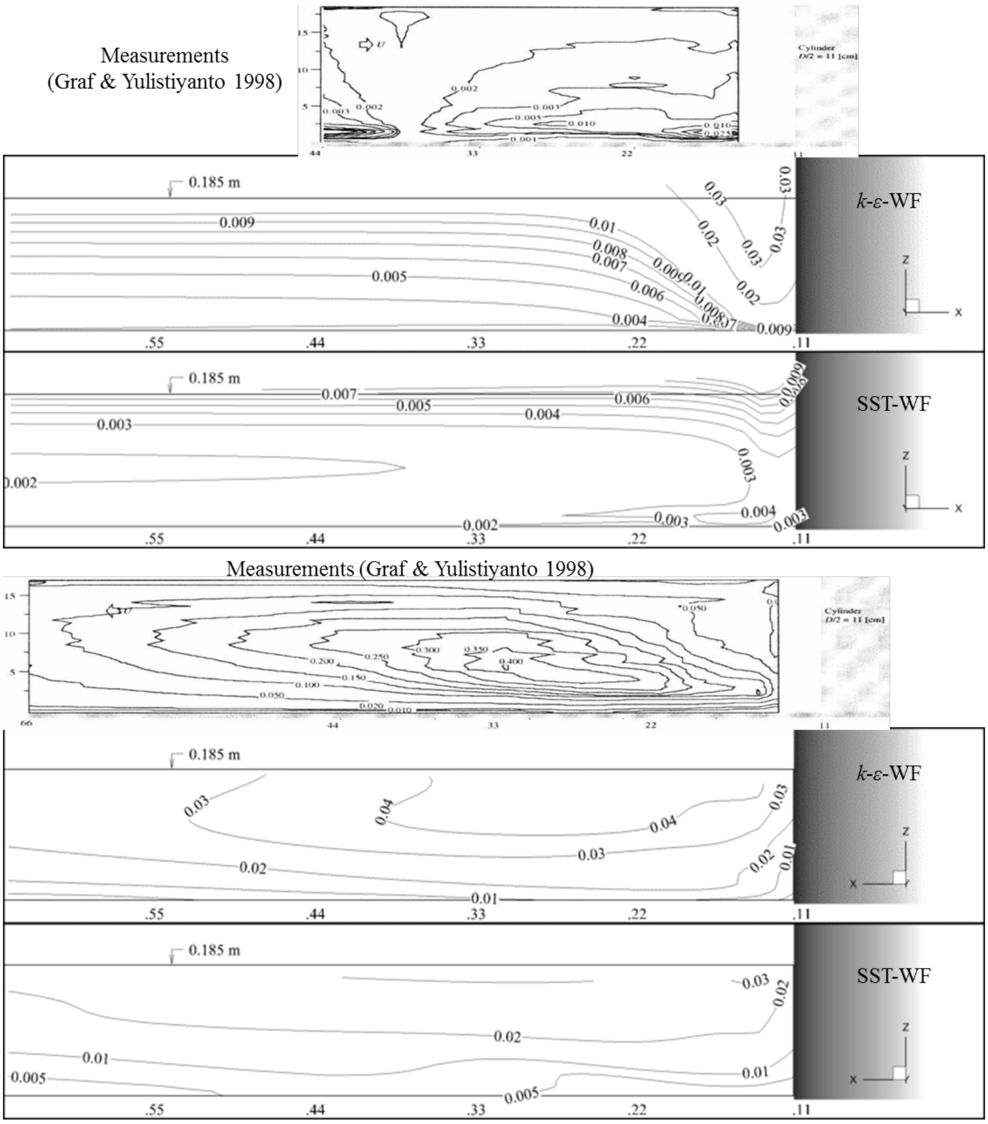

Figure 5. Comparison of measurement (Graf & Yulistiyanto 1998) and numerical predictions of the turbulent kinetic energy at the symmetric planes of [*upper*] upstream and [*lower*] downstream of the cylinder.

All URANS and SAS computations with wall functions appear to remarkably underestimate the TKE associated with the horseshoe vortex and the lee-wake vortices, as shown in Figure 5. In fact, it is already well known that this kind of performance of URANS computation (Apsley & Leschziner 2001). Even though it still underestimates the TKE, URANS with wall-integration through the viscous layer on WI mesh yields better solution than those obtained by using wall functions. Similar results are also observed in the solutions computed in the wake region. Our preliminary result of SAS-WI computation shows that the scale-resolving simulation works well to reproduce the mean flow field and the turbulent vortical structures with intense unsteadiness in the vicinity of the wall-mounted cylinder.

5 CONCLUSIONS

The present results show that numerical simulation accounting for the free-surface variation of turbulent flow around a free-surface-piercing circular cylinder results in the dramatic change of the mean flow features in the wake region. The present numerical results demonstrate that the resolving of the free-surface variation is an essential prerequisite to accurately capture the mean flow fields as well as the dynamic behavior of the lee-wake vortices downstream of the cylinder at the Froude number of 0.5. URANS computations employing wall functions can reasonably predict the time-averaged velocity vector fields, but significantly underestimate the turbulent kinetic energy distribution associated with the horseshoe vortex and the lee-wake vortices. The URANS simulation with wall integration of the viscous layer improves of the numerical prediction of the turbulence statistics. The URANS computations yield the quasi-steady-state flow fields in the vicinity of the obstacle regardless of the wall treatment, while the scale-adaptive simulation appears to well reproduce the large-scale instability of the lee-wake vortices.

ACKNOWLEDGEMENT

This work was supported by a grant (12-TI-C02) from Advanced Water Management Research Program funded by MLIT and a grand (2012M3A2A1050979) from Public Welfare & Security R&D Program through the NRF of Korea funded by MEST. Computational resources were supported by the Korea Supercomputing Center/KISTI (Grant No. KSC-2013-C2-058).

REFERENCES

Apsley, D. D. & Leschziner, M. A. (2001). Investigation of advanced turbulence models for the flow in a generic wing-body junction. *Flow, Turbulence & Combustion*, 67:25-55.

Escauriaza, C., Sotiropoulos, F. (2011). Lagrangian model of bed-load transport in turbulent junction flows. Journal of Fluid Mechanics, 666: 36-76.

Graf, W. H. and Yulistiyanto, B. (1998). Experiments on flow around a cylinder; the velocity and vorticity fields. *Journal of Hydraulic Research*. 36(4):, 637-654.

Devenport W.J. & Simpson, R.L. (1990). Time-dependent and time-averaged turbulence structure near the nose of a wing-body junction. *Journal of Fluid Mechanics,* 210: 23-55.

Egorov, Y., Menter, F. R., Lechner, R. and Cokljat, D. (2010). The scale-adaptive simulation method for unsteady turbulent flow predictions. Part 2L application to complex flows. *Flow, Turbulence & Combustion*. 85:139-165.

Kawamura T., Mayer, S., Garapon, A. and Sørensen L. (2002). Large eddy simulation of a flow past a free-surface piercing circular cylinder. *Journal of Fluids Engineering*, 124(3): 91-101.

Khosronejad A., Kang, S. & Sotiropoulos F. (2012). Experimental and computational investigation of local scour around bridge piers. *Advances in Water Resources*, 37: 73-85.

Kirkil, G., Constantiescu, G. & Ettema, R. (2009). Detached eddy simulation investigation of turbulence at a circular pier with scour hole. *Journal of Hydraulic Engineering*, 135(11): 888-901.

Liu, X. & García, M. H. (2008). Three-dimensional numerical model with free water surface and mesh deformation for local sediment scour. *J. Waterway, Port Coastal Ocean Eng*. 134(4): 203-217.

Lysenko D. A., Ertesvåg, I. S. & Rian, K. E. (2012). Large-eddy simulation of the flow over a circular cylinder at Reynolds number 3900 using the OpenFOAM Toolbox. *Flow, Turbulence & Combustion*. 89: 491-518.

Menter, F R. (1994). Two-equation eddy-viscosity turbulence models for engineering applications. *AIAA journal* 32(8): 1598-1605.

Menter, F. R., & Egorov, Y. (2010). The scale-adaptive simulation method for unsteady turbulent flow predictions. Part 1: theory and model description." *Flow, Turbulence & Combustion,* 85(1): 113-138.

Paik, J., Escauriaza, C. & Sotiropoulos, F. (2007). On the bimodal dynamics of the turbulent horseshoe vortex system in a wing-body junction. *Physics of Fluids*, 19, 045107.

Parnaudeau, P., Carlier, J., Heitz, D. & Lamballais, E. (2008). Experimental and numerical studies of the flow over a circular cylinder at Reynolds number 3900. *Physics of Fluids*, 20(8), 085101.

Rouland, A., Sumer, B. M., Fredsøe, J. & Michelsen, J., (2005). Numerical and experimental investigation of flow and scour around a circular pile. *Journal of Fluid Mechanics*, 534: 351-401.

Salaheldin T. M. Imran J. & Chaudhry M. H. (2004). Numerical modeling of three-dimensional flow field around circular piers. *Journal of Hydraulic Engineering*, 130(2): 91-100.

Spalart, P. R., Jou, W., Strelets, M. & Allmaras, S. (1997). Comments on the feasibility of LES for wings and on a hybrid RANS/LES approach. In: *Advances in DNS.LES*, 1st AFOSR Int. Conf. on DNS/LES.

Sumer, B. M., Christiansen, N. & Fredsøe, J. (1997). The horseshoe vortex and vortex shedding around a vertical wall-mounted cylinder exposed to waves. *Journal of Fluid Mechanics*, 332:41-70.

Weller, H.G. (2008). A new approach to VOF-based interface capturing methods for incompressible and compressible flow. *Technical Report* TR/HGW/04, OpenCFD Ltd.

Yu, G., Avital, E.J. & Willians, J.J.R. (2008). Large eddy simulation of flow past free-surface piercing circular cylinders. *Journal of Fluids Engineering*, 130: 101304-1--9.